Previously Published Works
UC Davis

A University of California author or department has made this article openly available. Thanks to the Academic Senate's Open Access Policy, a great many UC-authored scholarly publications will now be freely available on this site.
Let us know how this access is important for you. We want to hear your story!
http://escholarship.org/reader_feedback.html

Peer Reviewed

Title:
Understanding the Role of Solvation Forces on the Preferential Attachment of Nanoparticles in Liquid

Journal Issue:
ACS NANO, 10(1)

Author:
Welch, DA
Woehl, TJ
Park, C
Faller, R
Evans, JE
Browning, ND

Publication Date:
01-26-2016

Series:
UC Davis Previously Published Works

Permalink:
http://escholarship.org/uc/item/7w6302cp

DOI:
http://dx.doi.org/10.1021/acsnano.5b06632

Keywords:
molecular dynamics, in situ microscopy, nanoparticles, attachment

Local Identifier:
1588851

Copyright Information:
All rights reserved unless otherwise indicated. Contact the author or original publisher for any necessary permissions. eScholarship is not the copyright owner for deposited works. Learn more at http://www.escholarship.org/help_copyright.html#reuse

eScholarship
University of California

eScholarship provides open access, scholarly publishing services to the University of California and delivers a dynamic research platform to scholars worldwide.

Understanding the Role of Solvation Forces on the Preferential Attachment of Nanoparticles in Liquid

David A. Welch,[1*] Taylor Woehl,[2,†] Chiwoo Park,[3] Roland Faller,[4] James E. Evans,[5] Nigel D. Browning[6]

[1] Department of Chemical Engineering and Materials Science, University of California, Davis, One Shields Avenue, Davis, CA, 95616. E-mail: dawelch@ucdavis.edu

[2] Department of Chemical Engineering and Materials Science, University of California, Davis, One Shields Avenue, Davis, CA, 95616. E-mail: tjwoehl@gmail.com

[3] Department of Industrial and Manufacturing Engineering, Florida State University, Tallahassee, FL, 32310. E-mail: cpark5@fsu.edu

[4] Department of Chemical Engineering and Materials Science, University of California, Davis, One Shields Avenue, Davis, CA, 95616. E-mail: rfaller@ucdavis.edu

[5] Environmental Molecular Sciences Laboratory, Pacific Northwest National Laboratory, 902 Battelle Blvd, Richland, WA, 99354. E-mail: James.Evans@pnnl.gov

[6] Fundamental Computational Sciences Directorate, Pacific Northwest National Laboratory, 902 Battelle Blvd, Richland, WA, 99354. E-mail: Nigel.Browning@pnnl.gov

† Present address: Material Measurement Laboratory, National Institute of Standards and Technology, Boulder, CO, 80305.

*Address correspondence to David A. Welch, 1-509-578-0223, dawelch@ucdavis.edu

Abstract

Optimization of colloidal nanoparticle synthesis techniques requires an understanding of underlying particle growth mechanisms. Non-classical growth mechanisms are particularly important as they affect nanoparticle size and shape distributions which in turn influence functional properties. For example, preferential attachment of nanoparticles is known to lead to the formation of mesocrystals, although the formation mechanism is currently not well understood. Here we employ *in situ* liquid cell scanning transmission electron microscopy (STEM) and steered molecular dynamics (SMD) simulations to demonstrate that the experimentally observed preference for end-to-end attachment of silver nanorods is a result of weaker solvation forces occurring at rod ends. SMD reveals that when the side of a nanorod approaches another rod, perturbation in the surface bound water at the nanorod surface creates significant energy barriers to attachment. Additionally, rod morphology (*i.e.* facet shape) effects can explain the majority of the side attachment effects that are observed experimentally.

Keywords

molecular dynamics, *in situ* microscopy, nanoparticles, attachment

Luminescence, sensors, optical memory, catalysis, and various other areas have found novel uses for nanotechnological materials.[1] Silver nanoparticles in particular have applications in plasmonics,[2] drug delivery/biological labeling,[3] and chemical catalysis (*e.g.* for ethene oxidation).[4] Desirable properties of nanoparticles utilized in these applications stem from particle size and morphology (*e.g.* nanorod shapes are preferred for certain applications).[4-7] To obtain optimal properties, it is necessary to carefully control particle features during synthesis and ensure stability during use.[8] Particle coalescence is usually to be avoided due to its elimination of accessible particle surface area, but it can also be used to synthesize a desired particle network.[9, 10] It is one of many fundamental growth mechanisms and often occurs through the phenomenon of preferred attachment (*e.g.* "oriented attachment").[11] Through preferred attachment, preferred coalescence reactions between particle surfaces (*i.e.* at certain particle positions and orientations) result in specific particle structures. Such attachment effects are generally thought to be intricate results of van der Waals and Coulombic forces, including particle, ligand, and solvent interactions.[11] To provide an understanding of preferred nanoparticle attachment that can help guide the development of synthesis techniques, *in situ* TEM and SMD can be utilized in conjunction to both witness the preferential behavior of the nanoparticles and physically explain it.

Using *in situ* TEM, direct observation of nanoparticle growth and motion has been extensively performed.[12-26] Particle coalescence has been observed for haematite, iron oxyhydroxide, platinum-iron alloy, platinum, silver, and gold, allowing for assessment of coalescence features such as preferred particle orientations and kinetics.[12-14, 24-26] When performing these experiments, care must be taken to avoid electron beam artifacts, such as specimen charging/reduction, flow effects, and bubbles, that can influence specimen behavior.[18, 21, 22, 27, 28] However, recent experimental observations have shown that these effects can be quantified, controlled and mitigated using calibrated electron doses.[28-30] As a result, *in situ* TEM observations can be used as an accurate starting point for understanding nanoparticle behavior in liquids.

Simulations can serve as a source of understanding for the observed specimen behavior, and molecular dynamics (MD) simulations have been frequently applied to explain nanoparticle behavior.[31, 32] Aggregation and coalescence simulations have been performed, in the presence of solvent, for anatase, cadmium sulfide, and silver particles as well as for simpler model systems like Lennard-Jones and structureless particles.[33-38] These studies show the existence of solvation forces (aka a "solvent shield"[37]) that influence coalescence properties. For the case of coalescence between a silver nanocrystal and silver nanowire/nanoplate in a Lennard-Jones solvent, due to solvation effects, attachment was calculated to be particularly likely at particle ends.[35] In addition to solvation forces, electrostatic interactions owing to particle surface bound charge may play a role. Therefore, simple Hamaker or surface-energy models do not provide a complete physical description of coalescence, especially when particles are close.[11, 39] MD, on the other hand, attempts to give a complete description provided the model includes all relevant interactions.

In this work, we use SMD to explain *in situ* liquid cell STEM observations on end-to-end preferred attachment of silver nanorods in water.[13] SMD simulations reveal orientation-dependent solvation forces between nanorods. At rod sides, large energy barriers (> 15 kT) are generally found to prevent nanorod attachment, explaining the experimental distribution of attachment angles. These results highlight the role of the solvent in synthesis, and solvent-based effects are expected to explain preferred attachment behavior for various systems of dispersed nanoparticles.

Results and Discussion

In Situ Liquid Cell STEM of Nanoparticle Growth and Attachment

Silver nanoparticle growth and attachment processes were directly observed and initiated *via in situ* liquid cell STEM.[13, 40] Briefly, the liquid cell consists of a hermetically sealed microfluidic chamber comprised of two etched silicon chips coated with 50 nm thick electron transparent silicon nitride viewing windows. A 500 – 750 nm liquid precursor layer is sandwiched between the silicon chips. The imaging electron beam was used to simultaneously visualize and initiate silver nanoparticle growth from a dilute aqueous precursor solution of silver nitrate (0.1 mM) *via* electron beam induced reduction of the silver ions. Silver nanocrystals grew on the silicon nitride window surface, with their size increasing monotonically with time through monomer addition (of reduced silver ions) as well as aggregation of neighboring nanocrystals.[41] Further details on the experimental setup can be found in previous work[13, 20, 41] (see Methods section). For the experimental parameters used in this study, nanoparticles often grew into asymmetric shapes such as nanorods (Figure 1a, particle #2, cf. Movie #1 in Supplementary Data; rods had a mean aspect ratio of 2.1). The nanorods were characterized by a major axis (see the red arrows in Figure 1a) which changed direction as the nanoparticles grew, reoriented, and collided over times on the order of minutes. These mobile particles were observed to eventually attach to neighboring particles (cf. Movie #1). While previous studies focused on the mechanisms dictating individual nanoparticle growth[13] and the effect of aggregation on the nanoparticle size distribution,[41] here we focus on the mechanism dictating the attachment/coalescence of pairs of nanorods. The process of nanorod attachment is demonstrated in Figure 1a. Initially, two neighboring nanoparticles that were deposited on the membrane began to move relative to each other, sampling various configurations over a time of minutes. Eventually the nanoparticles collided in a favorable configuration and irreversibly attached (Figure 1a, middle panel). Following attachment, the two

nanoparticles often rearranged slightly before assuming their final attachment orientation, as shown by a change in the orientation of each nanorod's major axis direction (4th panel of Figure 1a).

To quantify the preferred attachment of the silver nanorods, we measured the orientation angles of several nanorod pairs directly after any post-attachment rearrangement. The orientation angle of a nanorod after attachment was defined to be the angle between the line defining its major axis and the line between its centroid and the point of attachment between the two nanorods (Figure 1b). This metric for orientation angle therefore yielded a measure of rod orientation for each nanorod in the pair, with values ranging from 0 to 90^{o}. The rod-rod angle was an additional metric and is defined to be the angle between the two major rod axes. Note that relative configurations for rod pairs can be described either by two orientation angles or by the combination of the rod-rod angle and one orientation angle. Figure 1c shows various possible attachment geometries along with corresponding orientation angles for each nanorod. For a statistically reliable analysis of the attachment process, we measured the orientation angles of 23 pairs of attached nanorods, taken from two separate *in situ* movies. A histogram of all the experimentally measured orientation angles shows a strong preference towards attachment at low orientation angle (*i.e.* at rod ends), with 85% of orientation angles being less than 45^{o} (Figure 1d). Figure 1e plots the orientation angle pairs of each attachment event (there being one angle per rod). A few outliers exist in this plot, but they typically consisted of one large orientation angle and one relatively small orientation angle, thus corresponding to an end-to-side attachment geometry (cf. Figure 1c). Taken together, the distribution of orientation angles and the pairwise orientation angles indicate a strong propensity for nanorods to attach in end-to-end configurations.

Modeling of Nanoparticle Attachment

In order to provide an understanding of the *in situ* TEM findings, we performed steered molecular dynamics (SMD) simulations of coalescence reactions to determine why attachment predominantly occurs at low orientation angles.[42] The SMD simulations (see Supplementary Methods) determined activation energies of the coalescence reactions as a function of relative rod configuration. For a given configuration of two deposited rods, the activation energy was determined by analyzing the integrated force acting on one rod as it was steered towards the other, stationary rod:

$$E_a = \int F(\mathbf{r})d\mathbf{r} \quad (1)$$

where $F(\mathbf{r})$ is the force acting on the steered rod, $\mathbf{r}$ is the position of that rod, and the range of integration is determined by a routine detailed in Supplementary Methods. In order to sample various orientation angles, for a given rod-rod angle, the tested point of coalescence effectively moved along the body of the stationary rod (from its side, at a 90° orientation angle, to its tip, at a 0° orientation angle). Simulation results for three selected rod-rod angles are shown in Figure 2. Coalescence is kinetically favorable at low orientation angle (*i.e.* at rod ends; orientation angle < 45°) according to the position of the activation energy minima. At high orientation angle (*i.e.* near the rod side and away from the end; orientation angle > 45°), large activation energies make rod attachment unlikely, and this trend is exemplified by approach C. These findings serve as an initial qualitative explanation as to why high orientation angle attachment was generally not observed in experiment.

Activation energies (see equation 1) are a result of various physical interactions taking place (between nanorods, solvent molecules, and the window membrane) as rods coalesce. The changes in metallic energy ($E_{metallic}$) and solvation energy ($E_{solvation}$) during coalescence were found to particularly contribute to the activation energy magnitude. Metallic energy is defined as the energy due to attractive many-bond interactions taking place between the rods' metal atoms (modeled in simulation with the

Sutton-Chen potential).[43] Solvation energy is defined as the energy due to generally repulsive two-body interactions taking place between one rod's metal atoms and the part of the water layer at that rod's surface that is in the vicinity of the other rod (see Supplementary Methods and Figure 3). By integrating forces determined from simulation trajectories for end-to-end, end-to-side, and side-to-side attachment (in a similar manner to equation 1; see Supplementary Methods), $\Delta E_{metallic}$ was calculated to be -9, -18, and -43 kT, respectively. Hence, when considering only rod-rod metallic interactions, side-to-side attachment would be expected to be the most common result in experiment. However, $\Delta E_{solvation}$ for end-to-end, end-to-side, and side-to-side attachment, was calculated to be -6, 53, and 158 kT, respectively. Thus, for attachments involving a rod side (*i.e.* a high orientation angle), the solvation energy change is about three times larger in magnitude than the metallic energy change, resulting in a significantly large activation energy. To further understand the nature of the solvation energy change, consider the solvation force-displacement curves in Figure 3 for end-to-end (*i.e.* tip) and side-to-side (*i.e.* side) coalescence. Large solvation forces during side coalescence were specifically due to repulsive atomic overlap between metal atoms and solvent atoms when silver-water bond lengths became compressed (by ~0.1 Å) upon rod approach. In general, the values of $\Delta E_{solvation}$ (which is due to perturbed water structure) and $\Delta E_{metallic}$ (which is due to many-bond interactions) are each highly sensitive to the relative configuration of the rod facets. These configuration-based sensitivities result in the sharp features seen in the activation energy landscapes in Figure 2.

We quantitatively determined coalescence reaction rates by combining calculated activation energies with a diffusion-based model of particle motion. Based on *in situ* STEM studies of silver nanoparticles grown in solution, we assume that particles were deposited on a TEM window and diffused in a manner similar to Brownian motion.[41] The corresponding translational diffusion coefficient determined from the rod trajectories is on the order of 1 nm^2/s, consistent with previous measurements of nanoparticle diffusion in liquid cells.[26, 41] The low diffusion coefficient is likely due to

interactions taking place around the particle-silicon nitride window interface. The rotational diffusion coefficient is also expected to be low.[26] We consider specifically the rate of coalescence reaction between aggregate nanorod pairs using Arrhenius kinetics of the form:

$$r = Ae^{-Ea/(kT)} \quad (2)$$

where r is reaction rate, A is frequency factor, E_a is activation energy, k is the Boltzmann constant, and T is temperature. We assume the distance that a rod in an aggregate must move towards another rod in order to react is about 0.2 nm (based on the length of the repulsive region in Figure 3; also see Supplemental Data). The frequency factor for such diffusive motion, assuming a diffusion coefficient of 1 nm^2/s, is on the order of 10/s. In order for a coalescence reaction to have a significant probability of occurring on the timescale of the experiment, we assume that the reaction rate must be greater than once per 48 hours. By this assumption, only reactions having $E_a < 15$ kT would be witnessed, and this is exclusively the case for attachment at low orientation angles (see Figure 2). Preferential attachment can thus be explained in terms of a kinetics model.

We tested rod-rod angles of 90, 70, 45, 30, and 20° with reduced sampling and size (see Supplementary Methods) to understand how coalescence proceeds for other possible configurations. Figure 4 shows the activation energy of side and end coalescence reactions as a function of rod-rod angle. Low energy barriers (< 15 kT) were predominantly found at rod ends. At a rod-rod angle of 30°, however, side coalescence had a low activation energy (~12 kT) and is thus more likely to occur on the timescale of the experiment. This low energy barrier appears to be due to a particular rod arrangement in which the facets of the rods are directed away from each other and, as a result, there are reduced water confinement effects. Compared to the experimental data, for six of twenty-three attachment events (see Figure 1e), at least one high orientation angle was found. Four of these attachment events were associated with rod-rod angles in the range of 22 to 43°, which is, in terms of the SMD model (see Figures 3 and 4), associated with low energy barriers due to relatively weak solvation forces. The two

remaining attachment events that are unaccounted for could be caused by deviations in particle shape or orientation (at the window membrane) from that in our model.

Quantitative accuracy in the SMD simulations of coalescence pathways is limited by the accuracy of the rod-rod and rod-solvent interaction potentials. Due to cutoff effects, these simulations did not take into account the attractive short-range (*i.e.* Lennard-Jones (LJ) and quantum Sutton-Chen (Q-SC)) interactions for atoms farther than 1 nm apart. An analysis of rod interactions comparing full LJ, cutoff LJ, cutoff Q-SC, or hybrid Q-SC-LJ interaction summation is given in Supplementary Data, indicating that our treatment of the rod-rod interaction is a good approximation. Aside from accuracy concerns, it is worth noting that the overall attractive rod-rod interaction becomes stronger for larger nanorods.[44] This increased attraction may not increase reaction rates, however, as we expect that larger nanorods exhibit an overall larger repulsive solvation force. Nonetheless, from analyzing experimental data, there is no clear trend for the effect of size on coalescence orientation.

The use of an ideal environment in the simulation with no electron beam effects included demonstrates the fundamental nature of preferred attachment in the liquid cell. For silver nanorods dispersed in salt solution (as opposed to pure water), we expect that the same general coalescence preferences result from similar solvent confinement effects occurring during nanorod approach. Due to beam charging effects, it is possible that the silver nanorods could obtain net, positive charges.[21, 28] As the nanorods are suspended in dielectric liquid, discharge into solution is expected. Based on the characteristic time scale for electrical discharge obtained from Maxwell's equations, the discharge time of a nanoparticle in a dilute electrolyte is on the order of nanoseconds.[45] Therefore, the nanoparticles in this case do not likely retain charge from the electron beam long enough to cause any significant electrostatic interparticle interactions.

Conclusions

Nanoparticle synthesis techniques benefit from *in situ* TEM techniques which observe and quantify particle growth mechanisms. Simulation techniques can in turn assist interpretation of the TEM results. In this work, an observed preference towards end-to-end attachment for silver nanorods has been analyzed, with 85% of the experimentally measured orientation angles corresponding to this attachment type. SMD simulations showed that solvation forces play an essential role in the preferred attachment mechanism. Due to solvation forces, activation energies (usually > 15 kT) kinetically hinder coalescence along the side of the rod, resulting in preferred attachment at rod ends. Of the remaining orientation angles that do not fit the trend of end-to-end attachment, the majority are explained by the discovery of a low activation energy to side attachment for a specific rod configuration that results in low solvation forces. Overall, the good agreement between the *in situ* findings and simulation results constructs a solvation force-based picture of preferred nanoparticle attachment.

Methods

***In situ* STEM**. *In situ* electron microscopy experiments of silver nanoparticle growth in aqueous environments were performed.[13] The fluid cell experimental apparatus was similar to that used in previous studies.[13, 20, 41] The *in situ* experiments were performed on a spherical aberration corrected JEOL JEM-2100F operating at 200 kV. The microscope was operated at a magnification of M = 100,000 x, image size of 512 x 512 pixels, 5 μs dwell time, and 7 pA beam current. Silver nanoparticles were grown from a dilute silver nitrate solution (0.1 mM) *via* electron beam induced reduction by aqueous electrons.[13] Movies of the nanoparticle growth and attachment were recorded at 2 fps using a freeware screen grabber.

Image Analysis. Details of the motion and coalescence of nanoparticles were extracted from

continuous capture STEM movies by our multiparticle tracking algorithm.[46] Further details are given in Supplementary Methods.

SMD. To understand observations of preferred attachment, steered molecular dynamics (SMD) simulations were used to calculate the kinetics of the attachment process.[42] Pairs of pentagonal silver nanorods, having specified relative configurations, were placed inside a model *in situ* STEM holder. This model consisted of two flat surfaces that represent the opposing window membranes, and 3000 to 6000 water molecules (in addition to the rods deposited at one membrane) were placed between them. Steered molecular dynamics calculations, using a pulling rate of 1 nm/ns, were performed with an in-house code. Irreversible work due to pulling was removed during post-simulation determination of activation energy. Potentials for water interactions with silver atoms and membrane surfaces were based on quantum mechanical data. Further details are given in Supplementary Methods.

Acknowledgments

We thank C. Mundy for helpful comments on the draft manuscript. This work was supported in part by the United States Department of Energy (DOE) Grant No. DE-FG02-03ER46057 through the University of California at Davis, the Laboratory Directed Research and Development (LDRD) Program: Chemical Imaging Initiative at Pacific Northwest National Laboratory (PNNL), and the Environmental Molecular Sciences Laboratory (EMSL), a national scientific user facility sponsored by the DOE's Office of Biological and Environmental Research and located at PNNL. PNNL is a multiprogram national laboratory operated by Battelle for the DOE under Contract DE-AC05-76RL01830. The development of the single particle tracking algorithm was supported by the National Science Foundation under NSF-1334012.

Supporting Information Available

Supplementary Methods: Details of image analysis and molecular dynamics methodology.

Supplementary Data: Analysis of the rod-rod potential and electrostatic treatment used in simulation.

Supplementary Movie 1: BF STEM movie of silver nanoparticle growth at M = 100,000 x, beam current of 7 pA, and a pixel dwell time of 5 μs. The pixel size is 3.13 nm/pix. The movie is displayed in real time with a frame rate of 1 fps.

This material is available free of charge via the Internet at http://pubs.acs.org

References

1. Kruis, F. E.; Fissan, H.; Peled, A. Synthesis of Nanoparticles in the Gas Phase for Electronic, Optical and Magnetic Applications - a Review. *J. Aerosol Sci*. **1998**, *29*, 511-535.
2. Rycenga, M.; Cobley, C. M.; Zeng, J.; Li, W.; Moran, C. H.; Zhang, Q.; Qin, D.; Xia, Y. Controlling the Synthesis and Assembly of Silver Nanostructures for Plasmonic Applications. *Chem. Rev.* **2011**, *111*, 3669-3712.
3. Doria, G.; Conde, J.; Veigas, B.; Giestas, L.; Almeida, C.; Assunção, M.; Rosa, J.; Baptista, P. V. Noble Metal Nanoparticles for Biosensing Applications. *Sensors* **2012**, *12*, 1657-1687.
4. Li, Y.; Liu, Q.; Shen, W. Morphology-Dependent Nanocatalysis: Metal Particles. *Dalton Trans*. **2011**, *40*, 5811-5826.
5. Yang, S.; Ni, X.; Yin, X.; Kante, B.; Zhang, P.; Zhu, J.; Wang, Y.; Zhang, X. Anisotropic Metal Nanoparticles: Synthesis, Assembly, and Optical Applications. *J. Phys. Chem. B* **2005**, *109*, 13857-13870.
6. Aiken, J. D. III; Finke, R. G. A Review of Modern Transition-Metal Nanoclusters: Their Synthesis, Characterization, and Applications in Catalysis. *J. Mol. Catal. A: Chem*. **1999**, *145*, 1-44.
7. Seyed-Razavi, A.; Snook, I. K.; Barnard, A. S. Origin of Nanomorphology: Does a Complete Theory of Nanoparticle Evolution Exist? *J. Mater. Chem*. **2010**, *20*, 416-421.
8. Watt, J.; Cheong, S.; Tilley, R. D. How to Control the Shape of Metal Nanostructures in Organic Solution Phase Synthesis for Plasmonics and Catalysis. *Nano Today* **2013**, *8*, 198-215.
9. Yu, X.; Wang, D.; Peng, Q.; Li, Y. Pt-M (M=Cu, Co, Ni, Fe) Nanocrystals: from Small Nanoparticles to Wormlike Nanowires by Oriented Attachment. *Chem. Eur. J*. **2013**, *19*, 233-239.
10. Lim, B.; Xia, Y. Metal Nanocrystals with Highly Branched Morphologies. *Angew. Chem. Int. Ed*. **2011**, *50*, 76-85.
11. Lv, W.; He, W.; Wang, X.; Niu, Y.; Cao, H.; Dickerson, J. H.; Wang, Z. Understanding the Oriented-Attachment Growth of Nanocrystals from an Energy Point of View: a Review. *Nanoscale* **2014**, *6*, 2531-2547.
12. Almeida, T. P.; Fay, M. W.; Zhu, Y.; Brown, P. D. *In Situ* TEM Investigation of β-FeOOH and α-Fe_2O_3 Nanorods. *Physica E* **2012**, *44*, 1058-1061.
13. Woehl, T. J.; Evans, J. E.; Arslan, I.; Ristenpart, W. D.; Browning, N. D. Direct *In Situ* Determination of the Mechanisms Controlling Nanoparticle Nucleation and Growth. *ACS Nano* **2012**, *6*, 8599-8610.

14. Liao, H.-G.; Cui, L.; Whitelam, S.; Zheng, H. Real-Time Imaging of Pt_3Fe Nanorod Growth in Solution. *Science* **2012**, *336*, 1011-1014.
15. Yuk, J. M.; Park, J.; Ercius, P.; Kim, K.; Hellebusch, D. J.; Crommie, M. F.; Lee, J. Y.; Zettl, A.; Alivisatos, A. P. High-Resolution EM of Colloidal Nanocrystal Growth using Graphene Liquid Cells. *Science* **2012**, *336*, 61-64.
16. Park, J.; Zheng, H.; Lee, W. C.; Geissler, P. L.; Rabani, E.; Alivisatos, A. P. Direct Observation of Nanoparticle Superlattice Formation by Using Liquid Cell Transmission Electron Microscopy. *ACS Nano* **2012**, *6*, 2078-2085.
17. Parent, L. R.; Robinson, D. B.; Woehl, T. J.; Ristenpart, W. D.; Evans, J. E.; Browning, N. D.; Arslan, I. Direct *In Situ* Observation of Nanoparticle Synthesis in a Liquid Crystal Surfactant Template. *ACS Nano* **2012**, *6*, 3589-3596.
18. Liu, Y.; Lin, X.-M.; Sun, Y.; Rajh, T. *In Situ* Visualization of Self-Assembly of Charged Gold Nanoparticles. *J. Am. Chem. Soc*. **2013**, *135*, 3764-3767.
19. Grogan, J. M.; Rotkina, L.; Bau, H. H. *In Situ* Liquid-Cell Electron Microscopy of Colloid Aggregation and Growth Dynamics. *Phys. Rev. E* **2011**, *83*, 061405.
20. Evans, J. E.; Jungjohann, K. L.; Browning, N. D.; Arslan, I. Controlled Growth of Nanoparticles from Solution with *In Situ* Liquid Transmission Electron Microscopy. *Nano Lett*. **2011**, *11*, 2809-2813.
21. White, E. R.; Mecklenburg, M.; Shevitski, B.; Singer, S. B.; Regan, B. C. Charged Nanoparticle Dynamics in Water Induced by Scanning Transmission Electron Microscopy. *Langmuir* **2012**, *28*, 3695-3698.
22. Noh, K. W.; Liu, Y.; Sun, L.; Dillon, S. J. Challenges Associated with *In-Situ* TEM in Environmental Systems: The Case of Silver in Aqueous Solutions. *Ultramicroscopy* **2012**, *116*, 34-38.
23. Kimura, Y.; Niinomi, H.; Tsukamoto, K.; García-Ruiz, J. M. *In Situ* Live Observation of Nucleation and Dissolution of Sodium Chlorate Nanoparticles by Transmission Electron Microscopy. *J. Am. Chem. Soc*. **2014**, *136*, 1762-1765.
24. Li, D.; Nielsen, M. H.; Lee, J. R. I.; Frandsen, C.; Banfield, J. F.; De Yoreo, J. J. Direction-Specific Interactions Control Crystal Growth by Oriented Attachment. *Science* **2012**, *336*, 1014-1018.
25. Zheng, H.; Smith, R. K.; Jun, Y.; Kisielowski, C.; Dahmen, U. Alivisatos, A. P. Observation of Single Colloidal Platinum Nanocrystal Growth Trajectories. *Science* **2009**, *324*, 1309-1312.
26. Lu, J., Aabdin, Z., Loh, N. D., Bhattacharya, D. & Mirsaidov, U. Nanoparticle Dynamics in a Nanodroplet. *Nano Lett*. **2014**, *14*, 2111-2115.
27. Egerton, R. F.; Li, P.; Malac, M. Radiation Damage in the TEM and SEM. *Micron* **2004**, *35*, 399-409.
28. Woehl, T. J.; Jungjohann, K. L.; Evans, J. E.; Arslan, I.; Ristenpart, W. D.; Browning. N. D. Experimental Procedures to Mitigate Electron Beam Induced Artifacts during *In Situ* Fluid Imaging of Nanomaterials. *Ultramicroscopy* **2013**, *127*, 53-63.
29. Abellan, P.; Woehl, T. J.; Parent, L. R.; Browning, N. D.; Evans, J. E.; Arslan, I. Factors Influencing Quantitative Liquid (Scanning) Transmission Electron Microscopy. *Chem. Commun*. **2014**, *50*, 4873-4880.
30. Schneider, N. M.; Norton, M. M.; Mendel, B. J.; Grogan, J. M.; Ross, F. M.; Bau, H. H. Electron-Water Interactions and Implications for Liquid Cell Electron Microscopy. *J. Phys. Chem. C* **2014**, *118*, 22373-22382.
31. Anwar, J.; Zahn, D. Uncovering Molecular Processes in Crystal Nucleation and Growth by Using Molecular Simulation. *Angew. Chem. Int. Ed*. **2011**, *50*, 1996-2013.
32. Tian, P. Molecular Dynamics Simulations of Nanoparticles. *Annu. Rep. Prog. Chem., Sect. C* **2008**, *104*, 142-164.
33. Raju, M.; van Duin, A. C. T.; Fichthorn, K. A. Mechanisms of Oriented Attachment of TiO_2

Nanocrystals in Vacuum and Humid Environments: Reactive Molecular Dynamics. *Nano Lett*. **2014**, *14*, 1836-1842.
34. Widmer-Cooper, A.; Geissler, P. Orientational Ordering of Passivating Ligands on CdS Nanorods in Solution Generates Strong Rod-Rod Interactions. *Nano Lett*. **2014**, *14*, 57-65.
35. Sathiyanarayanan, R.; Alimohammadi, M.; Zhou, Y.; Fichthorn, K. A. Role of Solvent in the Shape-Controlled Synthesis of Anisotropic Colloidal Nanostructures. *J. Phys. Chem. C* **2011**, *115*, 18983-18990.
36. Qin. Y.; Fichthorn, K. A. Molecular-Dynamics Simulation of Forces between Nanoparticles in a Lennard-Jones Liquid. *J. Chem. Phys*. **2003**, *119*, 9745-9754.
37. Verma, S. K.; Mukherjee A. K.; Sinha, I. Simulating Interactions between Nanoparticles in Lennard-Jones Liquids. *Chem. Phys. Lett*. **2013**, *572*, 85-89.
38. Shinto, H.; Miyahara, M.; Higashitani, K. Evaluation of Interaction Forces Between Macroparticles in Simple Fluids by Molecular Dynamics Simulation. *J. Colloid Interface Sci*. **1999**, *209*, 79-85.
39. Chun, J.; Mundy, C. J.; Schenter, G. K. Personal communication, 2015.
40. de Jonge, N.; Ross, F. M. Electron Microscopy of Specimens in Liquid. *Nature Nanotech*. **2011**, *6*, 695-704.
41. Woehl, T. J.; Park, C.; Evans, J. E.; Arslan, I.; Ristenpart, W. D.; Browning, N. D. Direct Observation of Aggregative Nanoparticle Growth: Kinetic Modeling of the Size Distribution and Growth Rate. *Nano Lett*. **2014**, *14*, 373-378.
42. Izrailev, S.; Stepaniants, S.; Isralewitz, B.; Kosztin, D.; Lu, H.; Molnar, F.; Wriggers, W.; Schulten, K. Steered Molecular Dynamics. In *Computational Molecular Dynamics: Challenges, Methods, Ideas, Volume 4 of Lecture Notes in Computational Science and Engineering*; Deuflhard, P., Hermans, J., Leimkuhler, B., Mark, A. E., Reich, S., Skeel, R. D., Eds.; Springer-Verlag: Berlin, 1998; pp 39-65.
43. Kimura, Y.; Qi, Y.; Çağın, T.; Goddard, W. III. *The Quantum Sutton-Chen Many-Body Potential for Properties of fcc Metals*; Caltech ASCI Technical Report 003; California Institute of Technology: Pasadena, 1998.
44. Lv, W.; Yang, X.; Wang, W.; Niu, Y.; Liu, Z.; He, W. An Energy Investigation into 1D/2D Oriented-Attachment Assemblies of 1D Ag Nanocrystals. *ChemPhysChem* **2014**, *15*, 2688-2691.
45. Saville, D. A. Electrohydrodynamics: the Taylor-Melcher Leaky Dielectric Model. *Annu. Rev. Fluid Mech*. **1997**, *29*, 27-64.
46. Park, C.; Woehl, T. J.; Evans, J. E.; Browning, N. D. Minimum Cost Multi-Way Data Association for Optimizing Multitarget Tracking of Interacting Objects. *IEEE Transactions on Pattern Analysis and Machine Intelligence* **2015**, *37*, 611-624.
47. Ni, C.; Hassan, P. A.; Kaler, E. W. Structural Characteristics and Growth of Pentagonal Silver Nanorods Prepared by a Surfactant Method. *Langmuir* **2005**, *21*, 3334-3337.
48. Hofmeister, H.; Nepijko, S. A.; Ievlev, D. N.; Schulze, W.; Ertl, G. Composition and Lattice Structure of Fivefold Twinned Nanorods of Silver. *J. Cryst. Growth* **2002**, *234*, 773-781.
49. Chen, H.; Gao, Y.; Yu, H.; Zhang, H.; Liu, L.; Shi, Y.; Tian, H.; Xie, S.; Li, J. Structural Properties of Silver Nanorods with Fivefold Symmetry. *Micron* **2004**, *35*, 469-474.
50. Zhou, Y.; Fichthorn, K. A. Internal Stress-Induced Orthorhombic Phase in 5-Fold-Twinned Noble Metal Nanowires. *J. Phys. Chem. C* **2014**, *118*, 18746-18755.
51. Humphrey, W.; Dalke, A.; Schulten, K. VMD: Visual Molecular Dynamics. *J. Molec. Graphics* **1996**, *14*, 33-38.
52. Dunn, J. H.; Lambrakos, S. G.; Moore, P. G.; Nagumo, M. An Algorithm for Calculating Intramolecular Angle-Dependent Forces on Vector Computers. *J. Comp. Phys*. **1992**, *100*, 17-24.
53. Zhou, Y.; Cook, M.; Karplus, M. Protein Motions at Zero-Total Angular Momentum: the Importance of Long-Range Correlations. *Biophys. J*. **2000**, *79*, 2902-2908.

54. Gale, J. D.; Rohl, A. L. The General Utility Lattice Program (GULP). *Mol. Simul*. **2003**, *29*, 291-341.
55. Bussi, G.; Donadio, D.; Parrinello, M. Canonical Sampling through Velocity Rescaling. *J. Chem. Phys*. **2007**, *126*, 014101.
56. Salameh, S.; Schneider, J.; Laube, J.; Alessandrini, A.; Facci, P.; Seo, J. W.; Ciacchi, L. C.; Mädler, L. Adhesion Mechanisms of the Contact Interface of TiO_2 Nanoparticles in Films and Aggregates. *Langmuir* **2012**, *28*, 11457-11464.
57. Glosli, J. N.; Philpott, M. R. Adsorption of Hydrated Halide Ions on Charged Electrodes. Molecular Dynamics Simulation. *J. Chem. Phys*. **1993**, *98*, 9995-10008
58. Butenuth, A.; Moras, G.; Schneider, J.; Koleini, M.; Köppen, S.; Meißner, R.; Wright, L. B.; Walsh, T. R.; Ciacchi, L. C. *Ab Initio* Derived Force-Field Parameters for Molecular Dynamics Simulations of Deprotonated Amorphous-SiO_2/Water Interfaces. *Phys. Status Solidi B* **2012**, *249*, 292-305.
59. Wu, Y., Tepper, H. L. & Voth, G. A. Flexible Simple Point-Charge Water Model with Improved Liquid-State Properties. *J. Chem. Phys*. **2006**, *124*, 024503.
60. Michaelides, A.; Ranea, V. A.; de Andres, P. L.; King, D. A. General Model for Water Monomer Adsorption on Close-Packed Transition and Noble Metal Surfaces. *Phys. Rev. Lett*. **2003**, *90*, 216102.
61. Carrasco, J.; Klimeš, J.; Michaelides, A. The Role of van der Waals Forces in Water Adsorption on Metals. *J. Chem. Phys*. **2013**, *138*, 024708.
62. Toxvaerd, S.; Dyre, J. C. Communication: Shifted Forces in Molecular Dynamics. *J. Chem. Phys*. **2011**, *134*, 081102.
63. Fennell, C. J.; Gezelter, J. D. Is the Ewald Summation Still Necessary? Pairwise Alternatives to the Accepted Standard for Long-Range Electrostatics. *J. Chem. Phys*. **2006**, *124*, 234104.
64. Spohr, E. Effect of Electrostatic Boundary Conditions and System Size on the Interfacial Properties of Water and Aqueous Solutions. *J. Chem. Phys*. **1997**, *107*, 6342-6348.
65. Leiva, E. P. M.; Vázquez, C.; Rojas, M. I.; Mariscal, M. M. Computer Simulation of the Effective Double Layer Occurring on a Catalyst Surface under Electrochemical Promotion Condition. *J. Appl. Electrochem*. **2008**, *38*, 1065-1073.
66. Hansen, J. S.; Schrøder, T. B.; Dyre, J. C. Simplistic Coulomb Forces in Molecular Dynamics: Comparing the Wolf and Shifted-Force Approximations. *J. Phys. Chem. B* **2012**, *116*, 5738-5743.
67. Dufner, H.; Kast, S. M.; Brickmann, J.; Schlenkrich, M. Ewald Summation Versus Direct Summation of Shifted-Force Potentials for the Calculation of Electrostatic Interactions in Solids: a Quantitative Study. *J. Comput. Chem*. **1997**, *18*, 660-676.
68. Árnadóttir, L.; Stuve, E. M.; Jónsson, H. Adsorption of Water Monomer and Clusters on Platinum(111) Terrace and Related Steps and Kinks: I. Configurations, Energies, and Hydrogen Bonding. *Surface Science*. **2010**, *604*, 1978-1986.

Figure Legends

Figure 1: Attachment statistics compiled from *in situ* liquid cell STEM movies. (a) Bright field liquid cell STEM images (image is false colored; nanoparticles are in green and outlined in white, with liquid background in blue) of an attachment event (see Supplementary Movie #1). The two nanoparticles rearranged and attached over a period of about two seconds, after which orientation

angles were measured. The scale bar is 100 nm. (b) Representative schematic of two rod shaped nanoparticles undergoing attachment. Each orientation angle is measured from the line connecting the nanoparticle's centroid (blue square) to the point of attachment (blue circle), and the line defining the major axis of the nanoparticle (red arrow). The rod-rod angle is measured from the two lines defining the major nanoparticle axes. (c) Various possible nanoparticle attachment geometries and their corresponding orientation angles. (d) Histogram of attachment count as a function of orientation angle for 23 attachment events (each event having two measured orientation angles), using data from two separate movies. (e) Distribution of orientation angle pairs over the 23 attachment events.

Figure 2: Coalescence activation energy vs. orientation angle, determined for three different rod approaches. Reactions having low activation energies (< 29 kT) were found only at sampled orientation angles less than 45°. Coalescence at the rod end is thus kinetically favorable. The snapshots of coalesced nanorods, from top to bottom, correspond with orientation angles of 18, 29, and 0°. Average standard error of the activation energy was 3 kT (see Supplementary Methods for error determination).

Figure 3: Solvation force-displacement curves caused by monolayer compression for tip and side coalescence reactions. Due to solvation forces, side coalescence reactions generally had larger activation energies than tip coalescence reactions. Forces were averaged over the simulations performed for a rod-rod angle of 0° and an orientation angle of 0° (tip) or 90° (side). Rod separation is the approximate distance between rods, with 0 Å being the distance at which rods coalesce. The inset image is of the side coalescence reaction at 0.6 Å rod separation, with water between the rods shown in red. The effective length of the repulsive region that kinetically hinders coalescence was ~1.6 Å. Average standard error of the force, for tip and side coalescence, was 5 and 14 kT/Å, respectively.

Figure 4: Activation energy of end attachment (*i.e.* orientation angle < 45°) or side attachment (*i.e.* orientation angle > 45°), determined for various rod-rod angles. Side attachment generally had much greater energy barriers than end attachment. Particularly large energy barriers to side attachment were found at 0° and 70°, and the smallest energy barrier was situated between them. The location of this low energy barrier agrees with the majority of experimental observations on side attachment. Shown values are the minimum activation energy calculated for coalescence over all sampled orientation angles in the specified range. Shown images are for side approach at rod-rod angles of 30° and 70°. The "critical activation energy" line at 15 kT indicates the activation energy that results in a reaction frequency of once per two days. Attachments having activation energies above this line are not likely to occur on the timescale of the experiment.

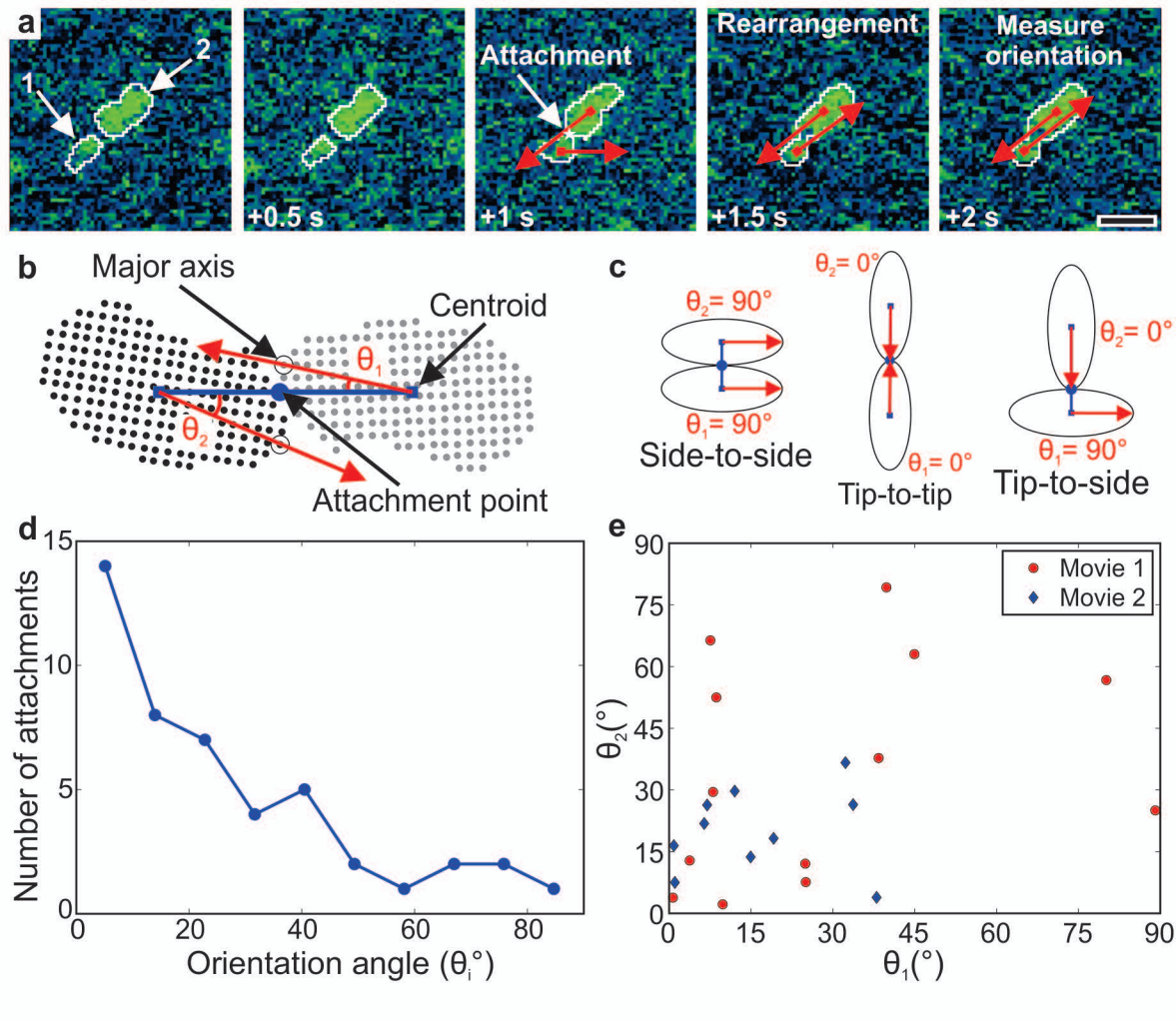
a
1
2
+0.5 s
Attachment
+1 s
Rearrangement
+1.5 s
Measure orientation
+2 s
b
Major axis
Centroid
θ1
θ2
Attachment point
c
θ2= 90°
θ1= 90°
Side-to-side
θ2= 0°
θ1= 0°
Tip-to-tip
θ2= 0°
θ1= 90°
Tip-to-side
d
Number of attachments
Orientation angle (θi°)
e
Movie 1
Movie 2
θ2(°)
θ1(°)

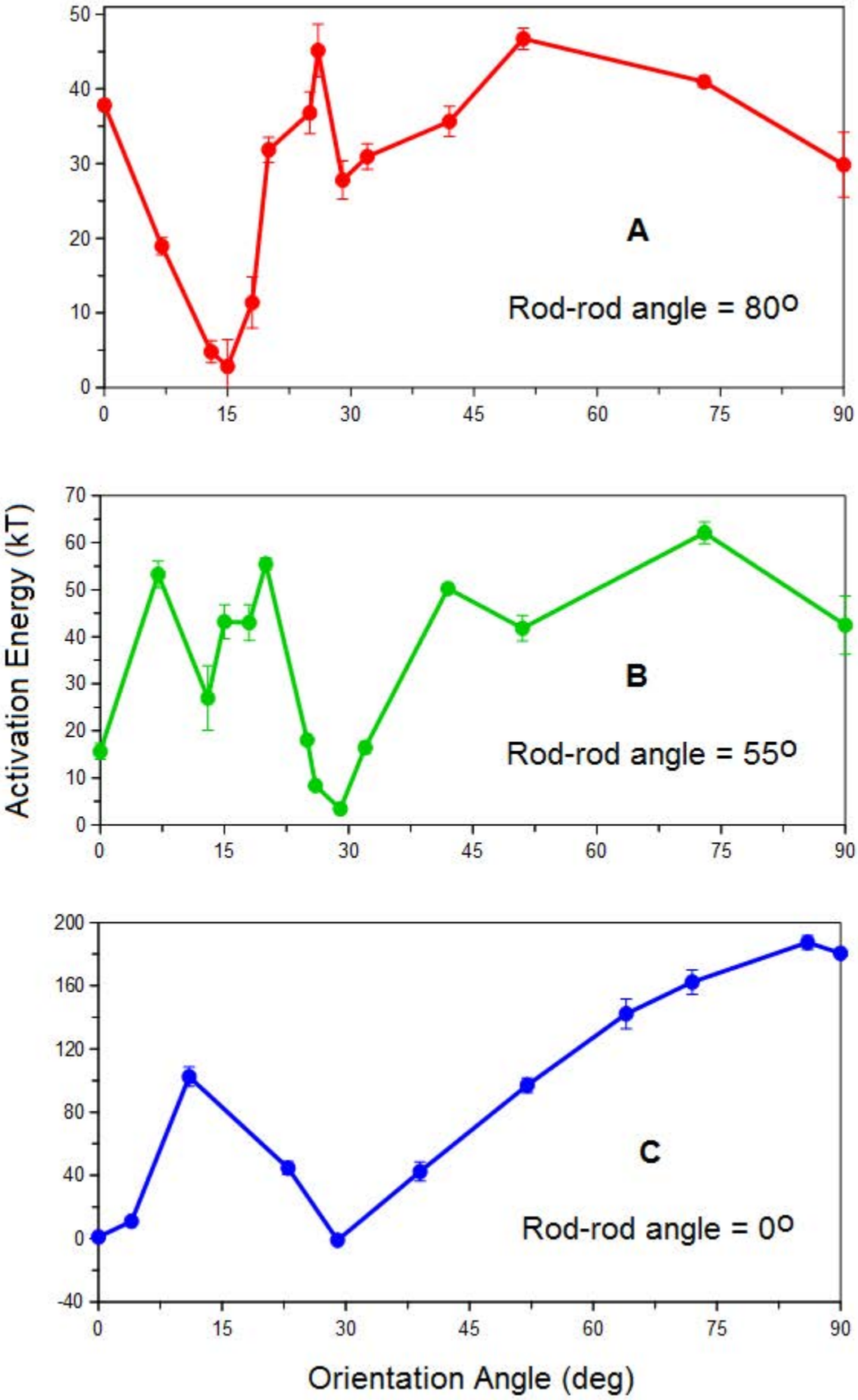
A
Rod-rod angle = 80°
B
Rod-rod angle = 55°
C
Rod-rod angle = 0°
Activation Energy (kT)
Orientation Angle (deg)

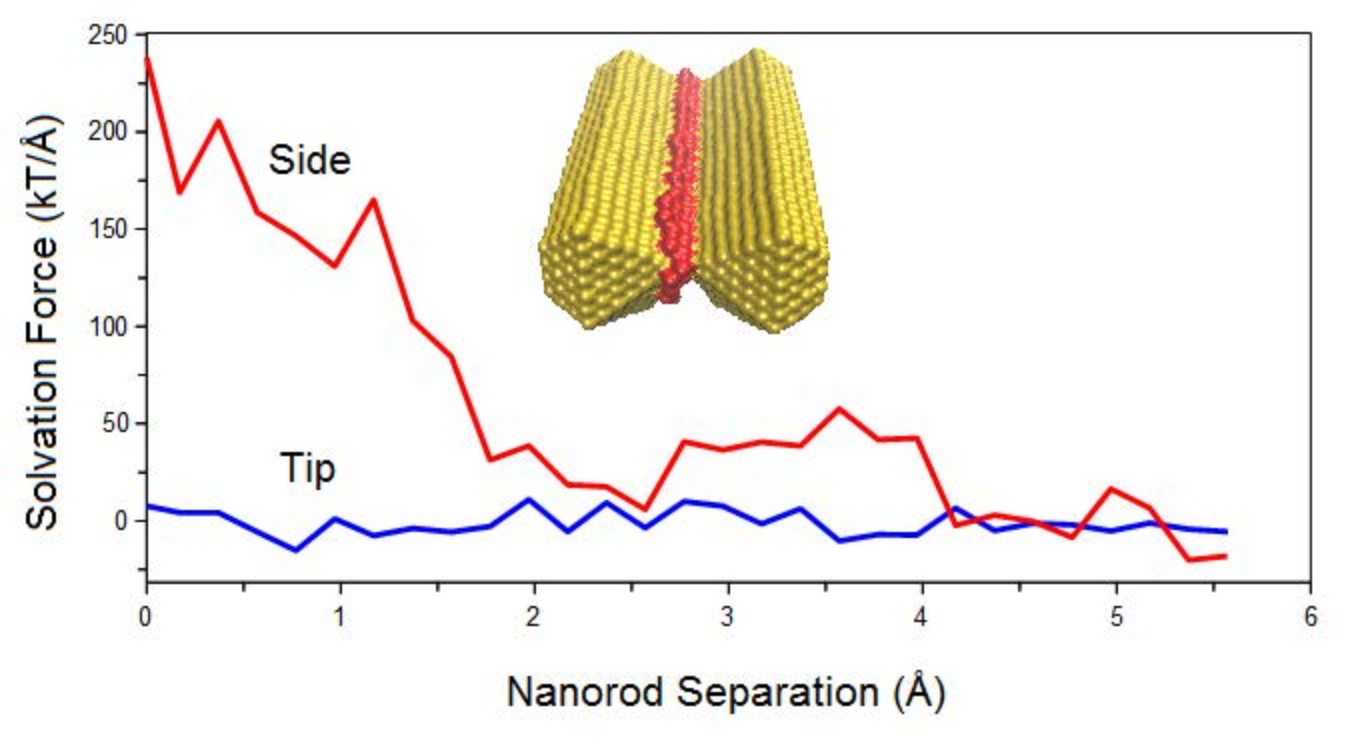
Solvation Force (kT/Å)
250
200
150
100
50
0
Side
Tip
0
1
2
3
4
5
6
Nanorod Separation (Å)

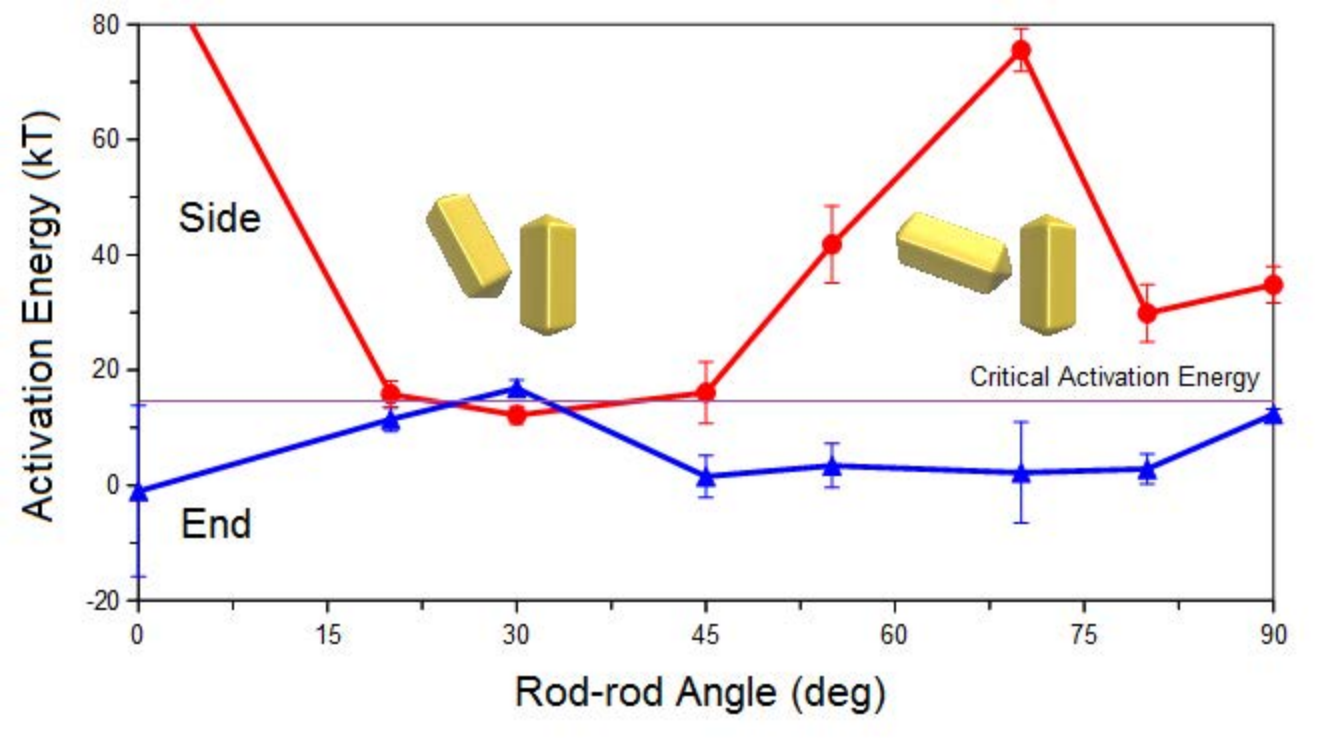
Activation Energy (kT)
80
60
40
20
0
-20
Side
End
Critical Activation Energy
0
15
30
45
60
75
90
Rod-rod Angle (deg)